SPACE WEATHER, VOL. ???, XXXX, DOI:10.1029/,

Decoding Solar Wind–Magnetosphere Coupling

M. J. Beharrell,[1] F. Honary,[1]

Abstract.

We employ a new NARMAX (Non-linear Auto-Regressive Moving Average with eXogenous inputs) code to disentangle the time varying relationship between the solar wind and SYM-H. The NARMAX method has previously been used to formulate a Dst model, using a preselected solar wind coupling function. In this work, which uses the higher resolution SYM-H in place of Dst, we are able to reveal the individual components of different solar wind-magnetosphere interaction processes as they contribute to the geomagnetic disturbance. This is achieved with a GPU-based NARMAX code that is around ten orders of magnitude faster than previous efforts from 2005, before general-purpose programming on GPUs was possible. The algorithm includes a composite cost function, to minimize over-fitting, and iterative re-orthogonalization, which reduces computational errors in the most critical calculations by a factor of $\sim 10^6$. The results show that negative deviations in SYM-H following southward IMF are firstly a measure of the increased magnetic flux in the geomagnetic tail, observed with a delay of 20-30 minutes from the time solar wind hits the bow shock. This piling up of magnetic flux corresponds to the substorm growth phase. Terms with longer delays are found which represent the dipolarization of the magnetotail, the injections of particles into the ring current, and their subsequent loss by flowout through the dayside magnetopause. Our results also indicate that the contribution of magnetopause currents to the storm time indices do not only depend on solar wind dynamic pressure, but also increase with solar wind electric field, $E = \mathbf{v} \times \mathbf{B}$. This is in agreement with previous studies that have shown the magnetopause is closer to the earth when the IMF is in the tangential direction.

1. Introduction

The interaction of the solar wind and earth's magnetosphere, beginning when an element of the solar wind impacts the dayside magnetopause, is a process that lasts several hours, evolving as the solar wind progresses around the magnetosphere. On the nightside, particles are injected into the ring current and accelerated as the magnetic field dipolarizes. The populations of these particles subsequently decay in a number of ways, including charge exchange with the upper atmosphere (particle precipitation) and flowout from the dusk and dayside magnetopause. Each stage of the interaction has a unique effect on Dst, a measure of the geomagnetic disturbance field on Earth.

There can be no doubt that the populations of energetic particles in the inner magnetosphere are enhanced during geomagnetic storms, nor that these particles contribute to negative excursions of the Dst index. To a first approximation the magnetic effect of the particles can be calculated with the Dessler-Parker-Sckopke (D-P-S) relation [*Dessler and Parker*, 1959; *Sckopke*, 1966], which is written in modern terms as

$$\mu \cdot \mathbf{b}(0) = 2U_K, \tag{1}$$

where $\mathbf{b}(0)$ is the (vector) average disturbance field over the surface of the earth, μ is the dipole moment, and U_K is the total kinetic energy of the plasma in the magnetosphere. The particles are primarily injected and accelerated on the nightside, as the tail magnetic field reconnects and relaxes to a more dipolar configuration. Traditionally a magnetic storm is considered to be a rapid succession of these dipolarization-injection events, which are called substorms. However, the findings of *Iyemori and Rao* [1996] appear to contradict this picture. They report that the Dst index decays (becomes less negative) after substorm onset. *Siscoe and Petschek* [1997] provides an explanation: during substorm onset the magnetic energy contained in the stretched magnetotail is transferred to charged particles in the ring current, but the stretched magnetotail itself has a Dst contribution, which is reduced during dipolarization. Further evidence of this is provided by *Lopez et al.* [2015], who report that, during the magnetic storm of 31 March 2001, SYM-H was observed to decrease by more than 200 nT without any ring current enhancement, but with growth of the magnetotail. During the storm, a large injection also coincided with a positive change (loss) in SYM-H. Earlier *Siscoe* [1970] had extended the D-P-S relation to include the magnetic field energy U_b,

$$\mu \cdot \mathbf{b}(0) = 2U_K + U_b, \tag{2}$$

The influence of the ring current kinetic energy on the disturbance field is twice that of the magnetic energy. This means that when the magnetotail dipolarizes, and magnetic energy from the tail is transferred to the ring current, there will be a decay in the Dst index if more than half of the magnetotail energy is lost elsewhere. On the other hand, if more than 50% of the energy stored in the tail is transferred to the ring current there will be an increase in -Dst. A substantial part of the magnetic energy transferred from the solar wind in the merging, convecting, and separating of the geomagnetic field and the IMF is lost downstream as a plasmoid during the substorm expansion process, and as Joule heating in the ionosphere. *Wang et al.* [2014] estimate that 13% of the solar wind kinetic energy is transferred to the magnetosphere. The input energy is roughly equally divided between the auroral ionosphere, the ring current, and the plasmoid [*Ieda et al.*, 1998; *Kamide and Baumjohann*, 1993]. The portion of energy that remains in the enhanced

[1]Physics Department, Lancaster University, UK. LA1 4WA.

ring current persists and builds up over the course of a geomagnetic storm.

Typically, the first change seen in Dst at the beginning of a storm is a positive swing, due to an increase in the dayside magnetopause current from an enhanced solar wind dynamic pressure. The injection of energetic particles into the ring current, resulting in prolonged negative Dst values, occurs primarily on the nightside. It takes time, of the order of an hour, for newly merged IMF and geomagnetic field lines to convect to the nightside of the planet and diffuse through the magnetotail, at which point the open geomagnetic field reconnects (closes), and undergoes dipolarization. Many formula are available that describe the negative excursions of Dst in terms of the solar wind parameters, some of these are listed in section 5. These "coupling functions" are often (incorrectly) assumed to directly represent the rate of particle injection into the ring current, but it is no coincidence that the functions appear to describe the rate of magnetic field merging on the dayside. Following the explanation of *Siscoe and Petschek* [1997], the merging of magnetic flux on the dayside results in a negative swing in Dst firstly due to the deformation of the magnetotail, and the enhanced cross-tail current. Around an hour later, when this merged flux reconnects on the nightside, the injection of particles into the ring current offsets the loss of Dst from the restored geomagnetic field. At this point the negative Dst contribution is transferred from the magnetic field to an enhanced ring current. Recently *Vasyliūnas* [2006] points out that the deformation of the geomagnetic tail can be represented by the amount of open (merged) magnetic flux, which is largely piled up in the magnetotail. If during tail reconnection the gain in -Dst from the ring current exactly cancels the loss from the reduced magnetotail contribution, then the coupling functions, which describe the enhancement of -Dst over the course of a storm, will be identical to the rate of dayside magnetic field merging. However, there is no reason to believe that exactly half of the magnetotail energy is transferred to the ring current, so that its contribution to Dst exactly replaces that of the deformed magnetotail.

The low time resolution of Dst has no doubt hampered past efforts to examine the coupling processes in detail. By using the higher resolution, but otherwise equivalent SYM-H [*Wanliss and Showalter*, 2006], we aim to discover formula describing changes in the disturbance magnetic field for each of the mechanisms described in this section. These include the magnetopause currents, magnetotail currents, magnetotail reconnection and particle injection, flowout through the magnetopause, and atmospheric charge exchange losses. To this end, we employ a new NARMAX code (Non-linear Auto-Regressive Moving Average with eXogenous inputs). NARMAX has previously been used to formulate a 1-hour resolution Dst model, using a preselected coupling function [*Boynton et al.*, 2011a]. The choice of coupling function, (described in *Boynton et al.* [2011b],) is made using the OLS-ERR (Ordinary Least Squares – Error Reduction Ratio) algorithm. OLS-ERR is commonly used to select NARMAX model terms; here it was used to choose between approximately 3600 candidate coupling functions. While the *Boynton et al.* [2011a] model provides a good approximation to Dst, the use of a single coupling function at 1-hour time resolution suggests that the function represents a mixture of the various coupling processes.

2. Theory

Some important physical processes in solar wind – magnetosphere coupling occur in timescales shorter than the 1 hour resolution of the Dst index. To pick apart the different mechanisms it is necessary to use the higher resolution SYM-H index. SYM-H is equivalent to Dst, but sampled at 1 minute resolution [*Wanliss and Showalter*, 2006]. The Burton-Mcpherron-Russell continuity equations for Dst [*Burton et al.*, 1975] can therefore be written in terms of SYM-H.

$$\text{SYM-H}^* = \text{SYM-H} - b\sqrt{p} + c, \tag{3}$$

$$\frac{\mathrm{d}\,\text{SYM-H}^*}{\mathrm{dt}} = Q - \frac{\text{SYM-H}^*}{\tau}, \tag{4}$$

where SYM-H* is a pressure-corrected SYM-H, ie with the Chapman-Ferraro (magnetopause) currents removed. To a first approximation b is usually assumed to be a constant, its value determined by the geometry of the dayside magnetopause. c is also assumed to be a constant. Q is a source term representing the injection of charged particles into the ring current, and SYM-H$^*/\tau$ represents an idealized exponential decay of the ring current. More recently it has become apparent that other important terms exist, and these should be added to the SYM-H continuity equation. Flowout, where particles entering the magnetosphere on quasi-trapped orbits drift out of the dayside magnetopause, is especially significant during storms [*Kozyra and Liemohn*, 2003]. Changes observed in Dst that are associated with the well known solar wind coupling functions, are commonly but incorrectly thought to be a direct measurement of Q, the injection of particles into the ring current. *Vasyliūnas* [2006] points out that the effects described by the coupling function are firstly due to the increasing magnetic flux in the magnetotail. Therefore, Dst and SYM-H must depend on the flux of open geomagnetic field lines, the majority of which are piled up in the magnetotail. The total rate of change of open magnetic flux can be written as the opening rate of flux on the dayside, minus the closing rate on the nightside.

$$\frac{\mathrm{d}\,\text{SYM-H}^*}{\mathrm{dt}} = Q + F - \frac{\text{SYM-H}^*}{\tau} - a\left(\frac{\mathrm{d}\,\Phi_\mathrm{d}}{\mathrm{dt}} - \frac{\mathrm{d}\,\Phi_\mathrm{n}}{\mathrm{dt}}\right), \tag{5}$$

where the coefficient a provides the conversion from magnetic flux in the tail to SYM-H on the ground; $\frac{\mathrm{d}\,\Phi_\mathrm{d}}{\mathrm{dt}}$ is the rate of flux opening on the dayside and piling up in the tail, and $\frac{\mathrm{d}\,\Phi_\mathrm{n}}{\mathrm{dt}}$ is the rate of flux closing in nightside reconnection. F is the rate of flowout from the dayside magnetopause. Note that the sign of Q is negative, as particles entering the magnetosphere increase -SYM-H, whereas F is positive.

Equation 5 is converted to use discrete time steps, Δt, and SYM-H is substituted for SYM-H* using equation 3,

$$\begin{aligned}
\text{SYM-H} - B_{-1} = {} & \left(1 - \frac{\Delta t}{\tau}\right)(\text{SYM-H}_{-1} - B_{-1}) && \text{(6a)}\\
& + b\,\Delta\sqrt{p} && \text{(6b)}\\
& - a\Delta\Phi_d && \text{(6c)}\\
& + (a\Delta\Phi_n + Q\Delta t) && \text{(6d)}\\
& + F\Delta t, && \text{(6e)}
\end{aligned}$$

where B ($= b\sqrt{p}$) is the best-known approximation of the pressure correction. It does not need to be highly accurate because the same value (B_{-1}) is deducted from both SYM-H and SYM-H$_{-1}$, and $\Delta t/\tau$ is small. This correction is applied to the SYM-H data before analysis begins. An initial run of the NARMAX code then provides a better value of $b\sqrt{p}$ from the term 6b. The analysis is re-run using the improved pressure correction as B. In our analysis b is not restricted to a constant. The NARMAX method searches for functions

based on the solar wind parameters to represent each of the terms 6a to 6e.

$\Delta\Phi_n$ is the amount of magnetic flux closed by magnetic reconnection on the nightside during the interval Δt. In equation 6 it is placed with Q, the injection of particles into the ring current, because both processes occur simultaneously and are difficult or impossible to separate empirically with analysis of solar wind and SYM-H data.

The physical processes linking variations in the solar wind to changes in SYM-H, such as the merging of flux on the dayside ($\Delta\Phi_d$), and nightside ($\Delta\Phi_n$), and enhancements in magnetopause currents ($\Delta\sqrt{p}$) each have different delays, or lags, relative to the arrival time of solar wind at the bow shock. For example, an increase in solar wind dynamic pressure results in an almost instantaneous increase in SYM-H, due to the magnetopause currents, but the closing of magnetic field lines on the nightside and accompanying injection of particles can lag by tens of minutes, as the magnetic field lines must first convect around the planet and diffuse into the tail. The differences in the lag times are exploited by the NARMAX model selection technique to decode the time series of SYM-H and solar wind data. In this paper a fast NARMAX code is used to find functions of solar wind parameters that best represent each of the 5 terms in equation 6.

3. Data

The solar wind data we use, spanning 1 January 1995 – 1 June 2013, is taken directly from the OMNI2 data set [*King and Papitashvili*, 2005]. Although solar wind data is available from as early as the 1960's, in an attempt to avoid possible bias from the varying sources we use only data from after 1995, which is provided by the newer ACE and WIND spacecraft. This has the additional benefit of reducing the size of the data set and speeding up the calculations. Data between 17 March 2000 and 9 May 2000 is excluded. This is a period with few data gaps, and is therefore ideal for validating the model. The OMNI2 magnetic field and plasma data has been time shifted to compensate for the location of the spacecraft, which are approximately 1 hour upstream of the Earth. The solar wind data is combined with SYM-H, and integrated to 5 minute samples.

It is advantageous to run the NARMAX algorithm on multiple subsets of the data. Comparing the results obtained for each subset shows the level of consistency of the model results, and reveals any over-fitting. Splitting the data set requires some care. If the data are split at a particular epoch there may be a bias in the results if, for example, the earlier data set is recorded during a different part of the solar cycle, or during a different season to the latter part of the data set. Separating the data set on a sample-by-sample basis is also problematic, as neighboring samples will be far from independent, and the two data sets will be nearly identical. Instead, the data is grouped into week-long segments, each containing 2016 samples (5 minute resolution). The week long segments are randomly distributed between two data sets: a training set, and a testing set. This method gives two independent and unbiased data sets, which are made as close in size as possible. The NARMAX algorithm is run on one of the two halves of data, while the other half is used to check the quality of the result as each term is selected. The model result is labeled '1A'. Next, the two subsets of data are switched around, with the training set becoming the testing set, and vice versa, and the result is labeled '1B'. The results 1A and 1B are based on separate data sets, ie no samples are used by the NARMAX code for both models 1A and 1B. The data randomization procedure is repeated, with the week-long segments again being distributed randomly between two new subsets of data. This time the results are labeled 2A and 2B. While 2A and 2B are produced using separate data sets, there is some overlap between the data used for 1A and 2B, for example. The procedure is repeated 5 times, giving a total of 10 NARMAX model results for comparison.

4. The NARMAX technique

The goal of the NARMAX method is to produce a model for a response variable, $y(t)$, in the form

$$y(t) = \sum_{k=1}^{M} p_k(t)\theta_k + \xi(t), \tag{7}$$

where t is the sample number (1,2,...,N), $p_k(t)$ is the k^{th} predictor out of a total of M, and θ_k is the coefficient of that predictor. $\xi(t)$ is the uncorrelated model residual, ie the part of $y(t)$ that cannot be represented by any of the predictor terms. In our case the output $y(t) = \text{SYM-H}^*(t)$, and each of the M predictor terms is a different product of the various solar wind parameters and SYM-H* values, with a range of lag times. For example, one of the parameters could be density × pressure at a lag of 10 minutes, and another could be SYM-H^{*2} × pressure^2 with a 15 minute lag. The NARMAX method seeks to identify the m most important predictors, (typically between 5 and 20,) and provide their coefficients. The number of candidate predictor terms, M, can clearly be very large when there are more than a few lags and solar wind parameters, so the candidates are limited to a particular degree of non-linearity (the sum of all of the powers in the product).

Simply ordering the candidate predictor terms by their correlation with $y(t)$, and selecting the top m, generally does a very poor job of model selection. With this naive approach the selected terms will tend to be strongly correlated with each other, and each will add very little additional information to the model. To produce an effective and efficient model it is far better to select predictors that each represent a unique aspect of the response variable. In other words, each variable should be selected based on the information it contains that is not present in any of the other selected terms. The NARMAX method achieves this by orthogonalizing the candidate predictor vectors, $\mathbf{p_k}$ with respect to the previously selected and orthogonalized predictor vectors, $\mathbf{w_1}, \mathbf{w_2}, ..., \mathbf{w_{k-1}}$.

In vectorized form, equation 7 can be written as

$$\mathbf{y} = \mathbf{P\Theta} + \mathbf{\Xi} \tag{8}$$

where $\mathbf{P}$ is a matrix formed by the candidate predictor vectors, with M columns and N rows. $\mathbf{\Theta}$ is the vector of coefficients. $\mathbf{P}$ can be decomposed into a product of an orthogonal matrix $\mathbf{W}$, and an upper triangle matrix $\mathbf{A}$.

$$\mathbf{P} = \mathbf{WA} \tag{9}$$

where,

$$\mathbf{W} = \begin{bmatrix} w_1(1) & w_2(1) & w_3(1) & \dots & w_M(1) \\ w_1(2) & w_2(2) & w_3(2) & \dots & w_M(2) \\ \vdots & \vdots & \vdots & \ddots & \vdots \\ w_1(N) & w_2(N) & w_3(N) & \dots & w_M(N) \end{bmatrix} \tag{10}$$

Every column of $\mathbf{W}$ is orthogonal to every other column, and each is a vector, $\mathbf{w_k}$, representing a time series of the k^{th} variable. It is not practical or necessary to compute the full orthogonal matrix $\mathbf{W}$, instead only the first m columns are filled with the $\mathbf{w_k}$ vectors that correspond to the best m predictors. These predictors are usually selected by the

NARMAX algorithm according to the value of the error reduction ratio, $[\mathrm{ERR}]_k$,

$$[\mathrm{ERR}]_k = \frac{(\mathbf{w}_k^T \mathbf{y})^2}{\mathbf{w}_k^T \mathbf{w}_k \;\; \mathbf{y}^T \mathbf{y}}. \tag{11}$$

At the k^{th} selection, the remaining candidates are each orthogonalized relative to the previously selected basis vectors, $\mathbf{w_1}, \mathbf{w_2}, ..., \mathbf{w_{k-1}}$. The candidate with the largest $[\mathrm{ERR}]_k$ is selected to be the k^{th} parameter. The selection process can be terminated when a desired tolerance, ρ, is reached

$$1 - \sum_{k=1}^{m} [\mathrm{ERR}]_k < \rho. \tag{12}$$

For a more complete description of the NARMAX model selection technique see eg *Billings* [2013] To improve the accuracy of the orthogonalization calculations in the NARMAX algorithm, iterative reorthogonalization [*Hoffmann*, 1989] is implemented, to ensure that the selected orthogonal vectors, $\mathbf{w_k}$, are precisely orthogonal. Testing showed this to produce an improvement in orthogonality of a factor of around 10^5 to 10^6, enabling the code to select the best terms even where there is a high level of ill conditioning.

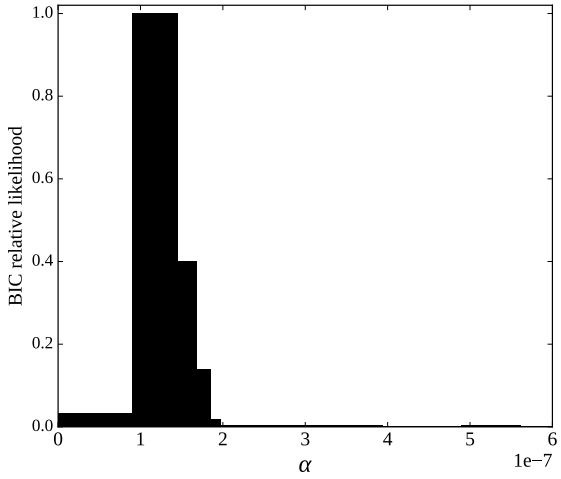

Figure 1. BIC derived relative likelihood of each NARMAX result, using data set 2A, as a function of the cost function α.

In an attempt to minimize over-fitting, a composite cost function is employed following the method of *Hong and Harris* [2001]. Its purpose is to penalize covariance between the selected parameters and minimize model prediction errors. The cost function, α, is a small positive scalar parameter that balances the model's approximation capability against its tendency to over fit the data. Instead of maximizing ERR, we maximize

$$\mathrm{ERR} - \alpha \left(\frac{N}{\mathbf{w}_k^T \mathbf{w}_k \;\; \mathbf{y}^T \mathbf{y}} \right). \tag{13}$$

When $\alpha = 0$ the algorithm is the identical to the more typical ordinary least squares ERR method. The NARMAX model selection is terminated when there are no more candidate predictors for which expression 13 is positive. Large α leads to no predictors being selected at all, since all are judged to have too high a variance. Although *Hong and Harris* [2001] do not provide a way to to automatically choose a reasonable value for α, it is possible to search all of α-space for the best result, since a range of α values will produce exactly the same NARMAX model. This is achieved by running the NARMAX code firstly with $\alpha = 0$, then with the smallest value of α, greater than the current value, that would produce a different model result. For each candidate predictor term, p_k, that was not selected, a corresponding α_k is calculated. α_k is the minimum value of α that would lead to p_k being the chosen regressor. The α_k that is closest to the current α is used for the next iteration of the model. For our data set it typically requires 15 to 20 values of α to cover the whole of α-space, from 0 to the value of α for which no terms are selected for the model.

The NARMAX code was implemented in OpenCL, and run on a single AMD Radeon R9 290X graphics card. OpenCL allows the algorithm to be programmed at a low level, with efficient use of the 2,816 stream processors, registers, caches, and 4 GB of on-board RAM. The code scales well, with each model run in this paper taking 1 to 14 hours. Extrapolating the CPU times given by *Billings and Wei* [2005] (their table 1) suggests a CPU time of the order of tens of millions of years to complete a single model run of the current work. Of course, some of this speed up, perhaps a factor of 1000×, is due to today's availability of fast and highly parallel GPUs, and the overall advances in computer performance over the last decade.

5. Parameter choices for model selection

The measurement parameters utilized in the NARMAX model are carefully chosen to ensure that the predictor variables are capable of reproducing equation 6. In order to accurately and precisely determine the unknown functions in the equation, a large range of exponents with small intervals are required in the candidate terms. The chosen measurement parameters are:

$$\begin{aligned} & |\mathrm{SYM\text{-}H}^*|^{1/2} \\ \Delta\sqrt{p}, \;\; & p^{1/3}, p^{1/12}, p^{-1/2} \\ & n^{3/2}, n^{1/3}, n^{1/12} \\ & E^{1/2}, E^{1/3}, E^{1/12} \\ & \sin\frac{\theta}{2}, \sin^4\frac{\theta}{2}, \end{aligned} \tag{14}$$

where E $(= vB_T)$, used throughout this paper, is the solar wind electric field in units of $\mathrm{mV \cdot m^{-1}}$; p is the dynamic solar wind pressure in nPa; n is the solar wind proton number density in $\mathrm{cm^{-3}}$; and θ is the IMF clock angle.

Lags of the solar wind parameters, ranging from 5 minutes to 4 hours, are added to the data set. To reduce computation time the longer lags are spaced at intervals. 5 to 60 minute lags are spaced at 5 minute intervals (i.e. without gaps), 60 to 120 minute lags are spaced at 10 minute intervals, and lags greater than 2 hours are spaced at 15 minute intervals.

Products of these parameters form the predictors in the NARMAX model, which are constructed up to a nonlinearity degree of 8. In other words, each candidate term in the NARMAX model comprises up to 8 of the measurement parameters multiplied together, with the same parameter able to appear more than once in each term. In forming the candidate predictor terms only solar wind parameters with the same lag are included in each term. A single 5 minute lag of the $|\mathrm{SYM\text{-}H}^*|^{1/2}$ parameter is included. This is combined in the candidate terms with solar wind parameters of any lag. For example, one of the candidate predictors will be $[|\mathrm{SYM\text{-}H}^*|^{1/2}(t-5\ \mathrm{m})]^3 \cdot [n^{1/3}(t-45\ \mathrm{m})]^1 \cdot [E^{1/2}(t-45\ \mathrm{m})]^2$.

In total there are 4,770,710 candidate predictors, including a constant term.

The NARMAX algorithm does not work with missing data, so any samples that contain missing data (in any of the lags from 0 minutes to 4 hours) are excluded. The remaining data comprises 1,175,732 samples.

Some examples of previously suggested coupling functions that are included in the candidate terms, with each of the aforementioned lags, are:

- *Kan and Lee* [1979]: $vB_T \sin^2 \frac{\theta}{2} = E^{1/2} \cdot E^{1/2} \cdot \sin \frac{\theta}{2} \cdot \sin \frac{\theta}{2}$ (non-linearity degree 4)
- *Wygant et al.* [1983]: $vB_T \sin^4 \frac{\theta}{2}$
- *Scurry and Russell* [1991]: $vB_T \sin^4 \frac{\theta}{2} p^{1/2}$
- *Temerin and Li* [2006]: $n^{1/2} v^2 B_T \sin^6 \frac{\theta}{2}$

These and many other variations of the coupling functions could be selected by NARMAX to be included in the model's approximation of equation 6. Similarly, the algorithm is able to choose different functions of the solar wind parameters for the other terms in equation 6. For example, if the coefficient b is better approximated by one of these functions, instead of a constant, that function will be selected. If the true Chapman Ferraro term is proportional to $\Delta \sqrt[3]{p}$, instead of $\Delta\sqrt{p}$, the model is able to select $\Delta\sqrt{p} \cdot p^{-1/2} \cdot p^{1/3}$ as a close approximation.

6. Results

The NARMAX selected model terms for the first run of the algorithm, 1A, are given in table 1. The first selected predictor term is 0.9945 SYM-H$^*(t - 5\,\mathrm{m})$. A model containing only this single term would be SYM-H$^*(t)$ = 0.9945 SYM-H$^*(t - 5\,\mathrm{m})$, which describes an exponential decay of SYM-H*, with a time constant of 15.1 hours. To a first approximation this model describes the decay of the ring current in the absence of energy input from the solar wind.

The standard method of measuring the significance of a term in NARMAX is with the Error Reduction Ratio (ERR). The higher the ERR value of a term, the closer it will allow the model to fit the data. The sum of ERR values approaches 1 as the the model becomes more complicated and fits the data more precisely. However, at some point the model will likely become over-fitted as new model terms are fitting to measurement errors instead of real physical processes. To address this, the relative likelihood of each term is calculated from the Bayesian Information Criterion (BIC), using the testing half of the data set, which is assumed to be independent of the training data used by the NARMAX code. The cumulative ERR, and relative likelihood at each step of the model selection are given in table 1. They indicate that the most likely model has 11 terms, with subsequent terms leading to over-fitting.

The composite cost function of *Hong and Harris* [2001] was employed, and the model was computed with a number of different values of the cost function, α. In all but one of our model runs, the model with $\alpha = 0$ provides the best fit to the testing data set, according the BIC. The single run that was improved with a non-zero cost function was run 2A. The relative likelihood of the models of run 2A, as a function of α, are shown in figure 1. Composite cost functions are an effective means of reducing over-fitting, and the reason they are not especially helpful here is because the data sets are large ($\sim 600,000$ samples, compared to 100 in the example given by *Hong and Harris* [2001]).

Of course, each 5 minute sample is not entirely independent of its neighbors. When calculating all BIC values an effective number of independent observations is used. Following *Zieba* [2010], this is calculated using the auto-correlation of SYM-H as $\frac{1}{50}^{\mathrm{th}}$ of the number of samples.

Most of the terms given in table 1 begin to look very familiar, as almost identical terms are seen in each of the 10 NARMAX runs. The terms are described briefly below, and in more detail in the next section.

The second most significant term chosen by the NARMAX algorithm has a positive coefficient, short lag time, and contains $\Delta\sqrt{p}$. These properties, which are also shared with terms 4 and 8, are associated with the Chapman-Ferraro (magnetopause) currents, corresponding to part b of equation 6.

Terms 3, 6, and 10 resemble the coupling functions listed in the previous section. They are functions of E and $\sin \frac{\theta}{2}$, with negative coefficients, and lag times that are consistent with the time it takes solar wind to transverse the magnetosphere, and pile up in the magnetotail. The negative coefficients means that an enhancement in the IMF – magnetosphere dayside merging rate will result in larger negative SYM-H values 20 to 30 minutes later. These terms represent part c of equation 6.

The fifth term appears to be essentially the geometric mean of the first term (a decay term) and the coupling function terms. The lag time associated with the coupling component is 90 minutes, which is approximately the time it takes merged magnetic field lines to transverse the magnetosphere, diffuse through the magnetotail and begin to reconnect. We associate this term with the loss of SYM-H as the open magnetic field in the magnetotail reconnects, injecting particles into the ring current. In this process energy is lost primarily by Joule heating in the ionosphere and in the plasmoid escaping down wind. This term represents part d of equation 6.

We are unable to attribute term 7 to any physical process. The decrease in the model's relative likelihood with

Table 1. Results from run 1A of the NARMAX code. The 11-term model has the highest likelihood, calculated by comparing the model results at each stage against a separate data set, using the Bayesian Information Criterion.

Term	Coefficient	Chosen parameters (lag times in parentheses)	Cumulative ERR	Relative likelihood
1	+0.9945	SYM-H*(5 m)	0.99840838	9.0×10^{-541}
2	+1.662	$\Delta\sqrt{p}\, E^{1/3} n^{2/3} p^{-1/2}$(5 m)	0.99853963	3.5×10^{-374}
3	−0.1220	$E^{3/4} p^{1/3} \sin^5 \frac{\theta}{2}$(25 m)	0.99864883	6.0×10^{-211}
4	+2.477	$\Delta\sqrt{p}\, E^{1/3} p^{1/12}$(0 m)	0.99874214	8.8×10^{-49}
5	+0.03593	$\lvert\text{SYM-H}^*\rvert^{1/2}$(5 m) $E^{1/3} p^{1/4} \sin^2 \frac{\theta}{2}$(90 m)	0.99875181	1.6×10^{-33}
6	−0.1598	$E^{5/6} p^{1/3} \sin^4 \frac{\theta}{2}$(20 m)	0.99875788	6.7×10^{-18}
7	−0.001384	$\lvert\text{SYM-H}^*\rvert^{1/2} \Delta\sqrt{p}\, E^{11/12} n^{3/2} p^{-1/2} \sin \frac{\theta}{2}$(5 m)	0.99876334	1.5×10^{-18}
8	+0.2777	$\Delta\sqrt{p}\, n^{3/2} p^{-23/12}$(10 m)	0.99876845	2.7×10^{-10}
9	−0.1789	$\Delta\sqrt{p}\, E^{5/6} n^{2/3} p^{-1/2} \sin^2 \frac{\theta}{2}$(15 m)	0.99877286	1.1×10^{-7}
10	−0.1184	$E^{11/12} n^{1/3} p^{-1/6} \sin^5 \frac{\theta}{2}$(30 m)	0.99877599	6.8×10^{-6}
11	+0.05670	$E n^{1/2} p^{-1/2} \sin^5 \frac{\theta}{2}$(150 m)	0.99877983	1
12	—	—	0.99878286	5.6×10^{-7}

Table 2. NARMAX model terms associated with solar wind dynamic pressure. These terms represent part b of equation 6.

Run	0 minute lag	5 minute lag	10 minute lag
1A	$+2.477\,E^{1/3}p^{1/12}\Delta\sqrt{p}$	$+1.662\,E^{1/3}n^{2/3}p^{-1/2}\Delta\sqrt{p}$	$+2.777\times10^{-1}\,n^{3/2}p^{-23/12}\Delta\sqrt{p}$
1B	$+2.115\,E^{1/2}\Delta\sqrt{p}$	$+1.472\,E^{1/2}n^{2/3}p^{-2/3}\Delta\sqrt{p}$	$+1.498\times10^{-1}\,n^{11/6}p^{-2}\Delta\sqrt{p}$
2A	$+2.080\,E^{5/12}p^{1/12}\Delta\sqrt{p}$	$+1.546\,E^{1/2}n^{2/3}p^{-2/3}\Delta\sqrt{p}$	$+2.571\times10^{-1}\,n^{3/2}p^{-11/6}\Delta\sqrt{p}$
2B	$+2.803\,E^{1/3}n^{-1/6}p^{1/4}\Delta\sqrt{p}$	$+1.634\,E^{1/3}n^{2/3}p^{-1/2}\Delta\sqrt{p}$	$+2.812\times10^{-1}\,n^{3/2}p^{-23/12}\Delta\sqrt{p}$
3A	$+2.474\,E^{5/12}\Delta\sqrt{p}$	$+1.665\,E^{5/12}n^{2/3}p^{-2/3}\Delta\sqrt{p}$	$+3.228\times10^{-1}\,n^{3/2}p^{-11/6}\Delta\sqrt{p}$
3B	$+2.069\,E^{5/12}p^{1/12}\Delta\sqrt{p}$	$+1.426\,E^{1/3}n^{2/3}p^{-1/2}\Delta\sqrt{p}$	$+2.577\times10^{-1}\,n^{3/2}p^{-23/12}\Delta\sqrt{p}$
4A	$+2.791\,E^{1/3}n^{-1/6}p^{1/4}\Delta\sqrt{p}$	$+2.025\,E^{1/3}n^{1/2}p^{-5/12}\Delta\sqrt{p}$	$+1.690\times10^{-1}\,n^{11/6}p^{-2}\Delta\sqrt{p}$
4B	$+2.307\,E^{5/12}\Delta\sqrt{p}$	$+1.645\,E^{5/12}n^{2/3}p^{-2/3}\Delta\sqrt{p}$	$+3.114\times10^{-1}\,n^{3/2}p^{-23/12}\Delta\sqrt{p}$
5A	$+2.715\,E^{1/3}n^{-1/6}p^{1/4}\Delta\sqrt{p}$	$+1.601\,E^{5/12}n^{2/3}p^{-2/3}\Delta\sqrt{p}$	$+3.142\times10^{-1}\,n^{3/2}p^{-11/6}\Delta\sqrt{p}$
5B	$+2.344\,E^{5/12}\Delta\sqrt{p}$	$+1.502\,E^{1/2}n^{2/3}p^{-2/3}\Delta\sqrt{p}$	$+2.738\times10^{-1}\,n^{3/2}p^{-23/12}\Delta\sqrt{p}$

Table 3. Traditionally referred to as coupling functions, these terms in the NARMAX model runs are associated with the merging of the IMF and geomagnetic field (part c of equation 6). The resultant open geomagnetic field is mostly within in the tail, causing SYM-H to become more negative due to enhanced magnetotail currents.

Run	20 minute lag	25 minute lag	Lags given in parentheses
1A	$-1.598\times10^{-1}\,E^{5/6}p^{1/3}\sin^4\frac{\theta}{2}$	$-1.220\times10^{-1}\,E^{3/4}p^{1/3}\sin^5\frac{\theta}{2}$	$-1.184\times10^{-1}\,E^{11/12}n^{1/3}p^{-1/6}\sin^5\frac{\theta}{2}(30\,\mathrm{m})$
1B	$-2.130\times10^{-1}\,E^{3/4}p^{1/3}\sin^4\frac{\theta}{2}$	$-1.564\times10^{-1}\,E^{11/12}n^{1/6}\sin^5\frac{\theta}{2}$	$-5.954\times10^{-2}\,En^{1/3}n^{1/3}p^{-1/12}\sin^5\frac{\theta}{2}(35\,\mathrm{m})$
2A	$-2.429\times10^{-1}\,E^{3/4}p^{5/12}\sin^5\frac{\theta}{2}$		$-1.423\times10^{-1}\,En^{1/3}p^{-1/6}\sin^5\frac{\theta}{2}(30\,\mathrm{m})$
2B	$-1.694\times10^{-1}\,E^{11/12}p^{1/4}\sin^5\frac{\theta}{2}$	$-2.476\times10^{-1}\,E^{3/4}p^{1/3}\sin^4\frac{\theta}{2}$	
3A	$-1.763\times10^{-1}\,E^{5/6}p^{1/3}\sin^5\frac{\theta}{2}$	$-1.272\times10^{-1}\,E^{5/6}p^{1/4}\sin^5\frac{\theta}{2}$	$-9.254\times10^{-2}\,En^{1/3}p^{-1/6}\sin^5\frac{\theta}{2}(30\,\mathrm{m})$
3B	$-2.451\times10^{-1}\,E^{3/4}p^{5/12}\sin^5\frac{\theta}{2}$		$-1.787\times10^{-1}\,E^{11/12}n^{1/6}\sin^4\frac{\theta}{2}(30\,\mathrm{m})$
4A	$-2.511\times10^{-1}\,E^{3/4}p^{5/12}\sin^5\frac{\theta}{2}$		$-1.795\times10^{-1}\,E^{11/12}n^{1/6}\sin^4\frac{\theta}{2}(30\,\mathrm{m})$
4B	$-1.866\times10^{-1}\,E^{5/6}p^{1/3}\sin^5\frac{\theta}{2}$	$-1.107\times10^{-1}\,E^{3/4}p^{1/3}\sin^4\frac{\theta}{2}$	$-1.326\times10^{-1}\,E^{11/12}n^{1/6}\sin^4\frac{\theta}{2}(30\,\mathrm{m})$
5A	$-2.372\times10^{-1}\,E^{3/4}p^{5/12}\sin^5\frac{\theta}{2}$		$-1.824\times10^{-1}\,E^{11/12}n^{1/6}\sin^4\frac{\theta}{2}(30\,\mathrm{m})$
5B	$-1.782\times10^{-1}\,E^{5/6}p^{1/3}\sin^5\frac{\theta}{2}$	$-2.273\times10^{-1}\,E^{3/4}p^{1/3}\sin^4\frac{\theta}{2}$	

Table 4. Model terms associated with tail reconnection, the loss of magnetotail flux, and the simultaneous injection of ring current particles. These terms represent part d of equation 6.

Run	Lag times given in parentheses	
1A	$+3.593\times10^{-2}\,E^{1/3}p^{1/4}\sin^2\frac{\theta}{2}(90\,\mathrm{m})\sqrt{\lvert\mathrm{SYM\text{-}H^*}\rvert}(5\,\mathrm{m})$	
1B	$+2.659\times10^{-2}\,E^{1/2}n^{1/6}\sin^3\frac{\theta}{2}(70\,\mathrm{m})\sqrt{\lvert\mathrm{SYM\text{-}H^*}\rvert}(5\,\mathrm{m})$	$+1.857\times10^{-2}\,E^{5/12}p^{1/4}\sin^2\frac{\theta}{2}(110\,\mathrm{m})\sqrt{\lvert\mathrm{SYM\text{-}H^*}\rvert}(5\,\mathrm{m})$
2A	$+1.863\times10^{-2}\,E^{7/12}p^{1/6}\sin^3\frac{\theta}{2}(70\,\mathrm{m})\sqrt{\lvert\mathrm{SYM\text{-}H^*}\rvert}(5\,\mathrm{m})$	$+1.714\times10^{-2}\,E^{1/3}p^{1/3}\sin^3\frac{\theta}{2}(90\,\mathrm{m})\sqrt{\lvert\mathrm{SYM\text{-}H^*}\rvert}(5\,\mathrm{m})$
2B	$+2.499\times10^{-2}\,E^{5/12}p^{1/4}\sin^2\frac{\theta}{2}(80\,\mathrm{m})\sqrt{\lvert\mathrm{SYM\text{-}H^*}\rvert}(5\,\mathrm{m})$	$+2.475\times10^{-2}\,E^{1/3}p^{1/3}\sin^2\frac{\theta}{2}(110\,\mathrm{m})\sqrt{\lvert\mathrm{SYM\text{-}H^*}\rvert}(5\,\mathrm{m})$
3A	$+2.680\times10^{-2}\,E^{5/12}p^{1/4}\sin^2\frac{\theta}{2}(80\,\mathrm{m})\sqrt{\lvert\mathrm{SYM\text{-}H^*}\rvert}(5\,\mathrm{m})$	$+2.484\times10^{-2}\,E^{1/2}p^{1/6}\sin^3\frac{\theta}{2}(120\,\mathrm{m})\sqrt{\lvert\mathrm{SYM\text{-}H^*}\rvert}(5\,\mathrm{m})$
3B	$+2.930\times10^{-2}\,E^{5/12}p^{1/4}\sin^2\frac{\theta}{2}(70\,\mathrm{m})\sqrt{\lvert\mathrm{SYM\text{-}H^*}\rvert}(5\,\mathrm{m})$	$+2.307\times10^{-2}\,E^{1/3}p^{1/3}\sin^2\frac{\theta}{2}(100\,\mathrm{m})\sqrt{\lvert\mathrm{SYM\text{-}H^*}\rvert}(5\,\mathrm{m})$
4A	$+2.776\times10^{-2}\,E^{1/3}n^{-1/6}p^{5/12}\sin^2\frac{\theta}{2}(60\,\mathrm{m})\sqrt{\lvert\mathrm{SYM\text{-}H^*}\rvert}(5\,\mathrm{m})$	$+2.080\times10^{-2}\,E^{1/3}p^{1/3}\sin^2\frac{\theta}{2}(90\,\mathrm{m})\sqrt{\lvert\mathrm{SYM\text{-}H^*}\rvert}(5\,\mathrm{m})$
4B	$+3.180\times10^{-2}\,E^{1/3}n^{-1/6}p^{5/12}\sin^2\frac{\theta}{2}(70\,\mathrm{m})\sqrt{\lvert\mathrm{SYM\text{-}H^*}\rvert}(5\,\mathrm{m})$	$+2.072\times10^{-2}\,E^{5/12}p^{1/4}\sin^2\frac{\theta}{2}(110\,\mathrm{m})\sqrt{\lvert\mathrm{SYM\text{-}H^*}\rvert}(5\,\mathrm{m})$
5A	$+2.670\times10^{-2}\,E^{5/12}n^{1/6}\sin^2\frac{\theta}{2}(70\,\mathrm{m})\sqrt{\lvert\mathrm{SYM\text{-}H^*}\rvert}(5\,\mathrm{m})$	$+1.771\times10^{-2}\,E^{1/3}p^{1/3}\sin^2\frac{\theta}{2}(110\,\mathrm{m})\sqrt{\lvert\mathrm{SYM\text{-}H^*}\rvert}(5\,\mathrm{m})$
5B	$+4.136\times10^{-2}\,E^{1/3}p^{1/4}\sin^2\frac{\theta}{2}(90\,\mathrm{m})\sqrt{\lvert\mathrm{SYM\text{-}H^*}\rvert}(5\,\mathrm{m})$	

the inclusion of this term indicates that it is anomalous. In other words, when this term is included the model becomes a worse fit for the testing data set.

Term 9 has a lag of 15 minutes. It represents a combination of two physical processes that overlap slightly in lag times: the Chapman-Ferraro current terms, with typical lags of 0 to 10 minutes; and the coupling function terms (3,6 and 10), which typically have 20 to 30 minute lag times. The overlap can be explained by the natural variation of lag times during different solar wind conditions. Lags will be shortened when the solar wind is fast. Errors in time-shifting of OMNI solar wind data from the L1 Lagrange point to Earth orbit may also increase the spread of lag times calculated for each process.

Term 11 has the longest lag of all of the NARMAX selected terms, at 150 minutes. It is similar in form to the dayside magnetic field merging (coupling) terms, but it has a positive coefficient indicative of a loss term. The rate of merging of the IMF and the geomagnetic field is expected to be proportional to the subsequent, delayed, injection of particles into the ring current. These particles drift from the nightside injection region to the dayside in approximately 1 hour. The lag of this term is 60 minutes longer than that of term 5, which is associated with the injection of particles into the ring current. It is likely that this term represents a first approximation of the flowout of ring current particles through the dayside magnetopause. This is part e of equation 6.

In the next sections we discuss each of the terms in more detail, and offer explanations for their forms.

7. Discussion

Tables 2, 3, 4, and 5 list all of the identified terms in each of the model runs. The consistency of the functions found using different sets of data provides a level of confidence in the results. Note that the coefficients alone do not represent the significance of each model term, because the functions vary. Figure 2 provides a schematic of the coupling mechanisms associated with these terms, and shows their respective lag times, relative to the moment an element of solar wind reaches the bow shock.

7.1. Charge exchange losses

In every model run the first predictor selected by the NARMAX algorithm is simply the 5 minute lag of SYM-H*. The coefficient of this term is slightly less than one, and therefore it represents an exponential decay in SYM-H.

It is identified as part a of equation 6. The mean exponential time scale, τ, given by the model runs is 17.6 hours, with a standard deviation of 2.2 hours. This loss term is primarily associated with charge exchange between ring current particles and the upper atmosphere, because, unlike other identified loss mechanisms described later, the rate of charge exchange depends on the overall number of particles in the ring current.

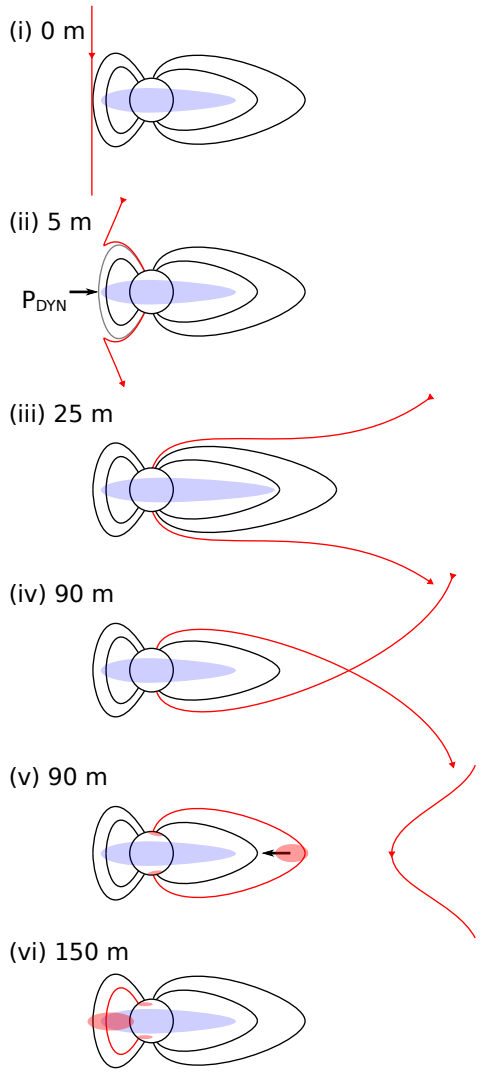

Figure 2. Schematic showing the physical processes identified in the NARMAX model terms, with the typical lag times. (i) An element of solar wind arrives at the dayside magnetopause. (ii) The IMF in that element merges with the geomagnetic field, while the solar wind dynamic pressure temporarily contributes to SYM-H via Chapman Ferraro currents. (iii) Open geomagnetic field piles up in the magnetotail, enhancing the tail current and -SYM-H. (iv) The open geomagnetic field has diffused throught the magnetotail and begins to reconnect. (v) Charged particles are injected into the ring current, as the magnetotail dipolarizes and the cross-tail current decays. Energy is lost from the magnetosphere in the plasmoid traveling down wind, and by ionospheric Joule heating. (vi) An hour after the ring current particles are injected from the magnetotail they reach the dayside, where those on pseudo-trapped orbits escape through the magnetopause, causing -SYM-H to decay.

Table 5. Model terms identified as ring current losses due to flowout. These terms appear in only 6 of the 10 model runs. They represent part e of equation 6.

Run	Lag times given in parentheses
1A	$+5.670 \times 10^{-2}\, En^{1/2}p^{-1/2} \sin^5 \frac{\theta}{2} (150\,\mathrm{m})$
1B	$+4.189 \times 10^{-2}\, E^{13/12}n^{1/2}p^{-1/2} \sin^4 \frac{\theta}{2} (135\,\mathrm{m})$
2A	$+5.567 \times 10^{-2}\, En^{1/2}p^{-1/2} \sin^5 \frac{\theta}{2} (150\,\mathrm{m})$
2B	
3A	
3B	
4A	$+5.998 \times 10^{-2}\, En^{1/2}p^{-1/2} \sin^5 \frac{\theta}{2} (135\,\mathrm{m})$
4B	$+5.966 \times 10^{-2}\, E^{5/6}n^{1/2}p^{-1/2} \sin^5 \frac{\theta}{2} (150\,\mathrm{m})$
5A	$+7.073 \times 10^{-2}\, E \sin^6 \frac{\theta}{2} (135\,\mathrm{m})$
5B	

7.2. Currents induced by solar wind pressure

Table 2 gives the model terms identified with currents produced by the solar wind dynamic pressure acting on the magnetosphere, for each of the 10 model runs. All are significant terms in the NARMAX models. They each contain $\Delta\sqrt{p}$, have lags of 10 minutes or less, and the coefficients are all positive. All three of the terms from a model run, added together, represent part b of equation 6.

The 0 minute lag represents Chapman Ferraro (magnetopause) currents on the dayside magnetosphere, since this is the time when a particular element of the solar wind reaches Earth. Alongside the expected $\Delta\sqrt{p}$ parameter, the 0-lag terms consistently contain the electric field, E, raised to the power 1/3 to 1/2. This is not surprising because the magnetopause is up to 1 R_E closer to Earth when the IMF in oriented in the YZ plane (ie perpendicular to the solar wind velocity) [*Dusik et al.*, 2010].

In some of the runs p appears with a small positive power in the 0-lag result, indicating that $\Delta\sqrt{p}$ might not be ideal, with the true power of p being slightly larger than 0.5. Three of the other runs contain $n^{-1/6}p^{1/4}$, which can be written as $p^{1/12}v^{1/3}$, so they contain the same small-powered pressure factor, with an additional velocity contribution. Although it appears that v has a greater contribution in these terms, the power of $E(= vB_T)$ is smaller, and it is actually the contribution from B_T that is less significant.

The 10 minute lag terms are very different to the 0 minute lags. They contain two factors, $n^{3/2}$ and p^{-2}. The 10 minute lags correspond to the time it takes the solar wind to pass the Earth and begin to apply pressure to the magnetotail. It is tempting to associate $n^{3/2}$ with an enhanced plasma sheet density, and p^{-2} with a cross-tail current that moves towards or away from Earth with the varying solar wind dynamic pressure, an effect suggested by *McPherron and O'Brien* [2001] to affect Dst. However, the two factors when combined are approximately equivalent to a large inverse power of velocity (v^{-4}), meaning that this term is significantly more important when the solar wind velocity is small. It remains a possibility that $\approx$ 10 minute errors in the time shifting of OMNI data during periods of low solar wind velocity could be responsible for the 10 minute lag terms, but if the time shifting is correct, then the above explanation is plausible. The 5 minute lag terms are simply a combination of the 0 lags and 10 minute lags.

7.3. Open magnetic flux

Two to three terms resembling the well known coupling functions are present in each model run. They are listed in table 3, and represent part c of equation 6. Some examples of previously suggested coupling functions are given in section 5 for comparison. Each of these were available, among the 4.8 million candidate terms, to the NARMAX code, with lags of up to 4 hours. The NARMAX selected

terms all have negative coefficients, and lags between 20 and 30 minutes. The functions closely resemble the rate of dayside merging of solar wind and geomagnetic field (see eg *Vasyliūnas* [2006]). All of the properties match expected changes in SYM-H from the piling up of open magnetic flux in the magnetotail and the corresponding enhancement of the cross tail current, which results in an increase of -SYM-H.

Terms with 20 minute lags are present in every model run. They are of the form $-E^{x_1}p^{x_2}\sin^{x_3}\frac{\theta}{2}$, where $x_1 = 9/12$ to $11/12$, $x_2 = 3/12$ to $5/12$, and $x_3 = 4$ to 5. The coupling function of *Temerin and Li* [2006] can be written $E_{\mathrm{T\&L}} = Ep^{1/2}\sin^6\frac{\theta}{2}$, so the 20 minute lag terms are equivalent to $E^{5/6}_{\mathrm{T\&L}}$. At longer lag times the same E and $\sin\frac{\theta}{2}$ dependencies remain, but the terms contain increasing powers of $1/v$. These $1/v$ contributions are less pronounced than in the 10 minute lag pressure terms in the previous section, and it is unclear if they are both a product of errors in the time shifting of OMNI data at low solar wind speeds.

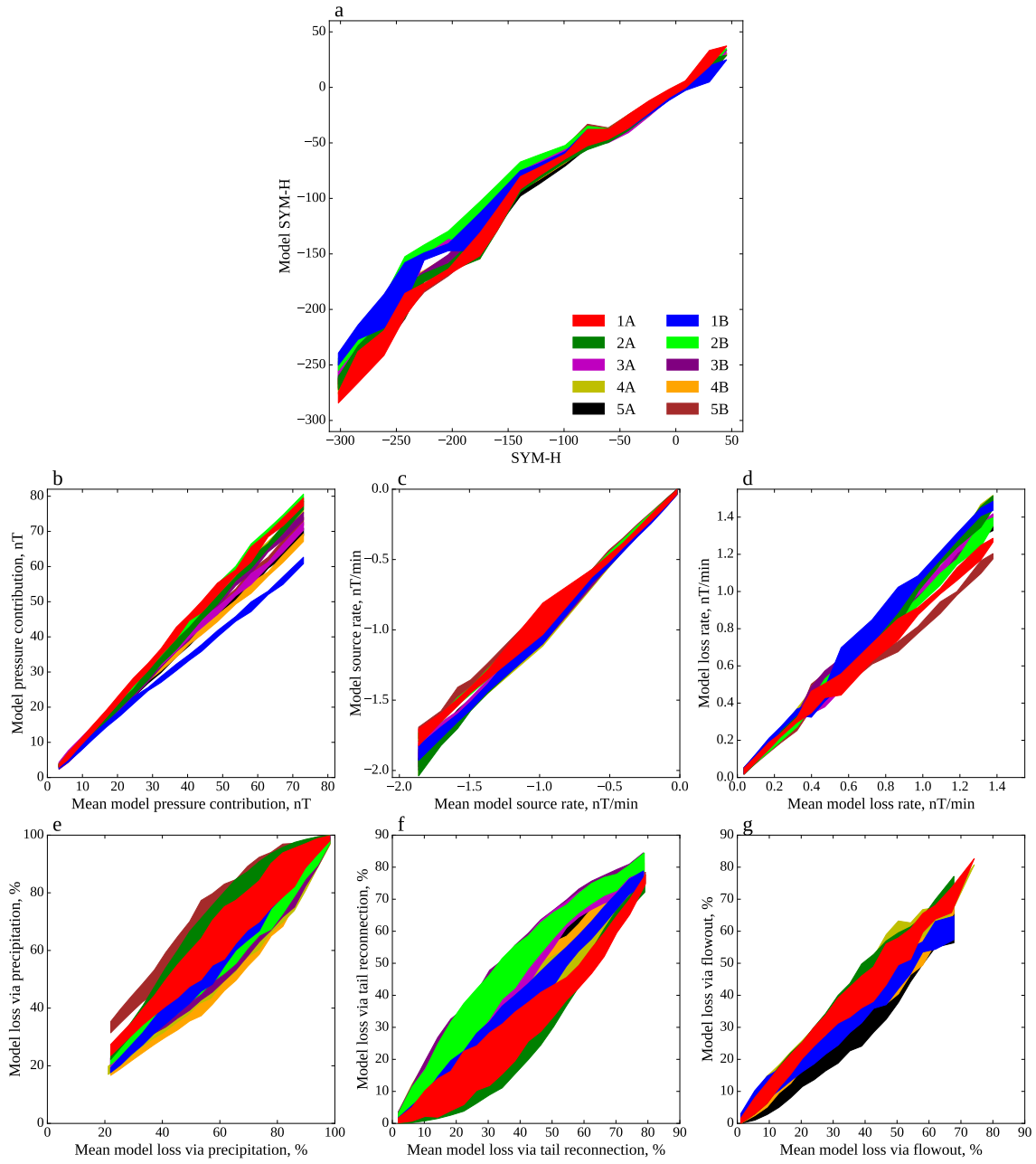

Figure 3. The variation between model runs. Panel *a* shows the model SYM-H from each run against the corresponding SYM-H observations. The samples are binned according to observed SYM-H, with a minimum of 12 samples per bin. The colored patches span the 25^{th} to the 75^{th} percentile, ie. half of the model samples are within the patches. For panels *b* – *g*, direct observations of the parameters are not possible, so the mean value from the model runs is used for the x-axes. Panel *b* shows the contribution to SYM-H from magnetopause currents (see table 2). Panel *c* shows the magnitude of the source terms (see table 3), and panel *d* shows the loss terms. The loss rates are broken down in panels *e*, *f* and *g*, corresponding to losses via particle precipitation (τ in equation 6), tail reconnection (table 4), and flowout (table 5), respectively.

7.4. Tail reconnection and particle injection

Typically around an hour after open magnetic flux enters the magnetotail, it has diffused through the tail to the point of reconnection. As the magnetic field dipolarizes following reconnection, charged particles are simultaneously injected into the ring current. This process is represented by part d of equation 6, and the associated model terms are given in table 4. Although the NARMAX model describes steady, continuous reconnection, in nature it tends to be bursty. The piling up of magnetic flux in the tail corresponds to the substorm growth phase, and the bursts of reconnection and particle injection are substorm expansion. The timing of substorms is very difficult, if not impossible, to predict using solar wind parameters alone, and it is not clear how much the model represents a smoothed time-average over the bursty events, or how much it represents steady tail reconnection occurring between the substorms. The increase in ring current particles enhances -SYM-H, whereas the loss of magnetic flux in the tail reduces -SYM-H. According to *Siscoe and Petschek* [1997], the contribution to SYM-H from energy in the ring current is twice that of energy stored in the magnetotail. This means that if all of the energy stored in the magnetotail is converted to ring current energy then -SYM-H should increase. The positive sign of the terms indicate that most of the energy is lost to other processes. This is in agreement with a statistical study of the substorm expansion energy budget by *Tanskanen* [2002], which gives figures of 30% for each of charged particle precipitation, Joule heating, and the escaping plasmoid, with the remaining 10% going to the ring current.

The functions identified with tail reconnection appear to be the geometric means of the near-instantaneous SYM-H*, and the dayside magnetic field merging delayed by between 60 and 120 minutes. It could be that these terms are the closest approximations, among the 4.8 million candidates, to a geometric combination of the merged flux reaching the tail reconnection point (70 to 110 minutes after merging on the dayside), and the instantaneous magnetic pressure in the tail, which is driving the reconnection. Although SYM-H* is itself a combination of ring current and magnetotail flux contributions, there is no better candidate term that represents only the instantaneous open magnetic flux in the tail.

7.5. Flowout

Terms in the NARMAX results identified as flowout (table 5) are the least significant among the coupling processes. They are only present in the results of 6 out of 10 runs. The functions superficially resemble the rate of magnetic field merging, but all except one depend only on the IMF, and can be written as $B_T \sin^5 \frac{\theta}{2}$. The lag times of 135 to 150 minutes are around an hour longer than the lag for particle injection into the ring current, which is consistent with the typical time it takes the bulk of injected particles to drift from the nightside injection region to the dayside magnetopause.

The difficulty in finding these functions with NARMAX could be because there are simply no good candidate terms that accurately describe the flowout rate. The actual flowout rate is expected to depend on the current location of the magnetopause, and the one-hour lagged charged particle injection rate. However, as we have seen, the rates of tail reconnection and particle injection will depend on SYM-H* at that time (one hour ago), and dayside merging 90 minutes before that. Allowing multiple different lags of the solar wind parameters in each term results in far too many candidates than can be processed by the NARMAX code in any reasonable amount of time.

7.6. Division of energy between loss processes

Over long timescales (ie the whole data set), approximately 49% of the overall loss of SYM-H in the NARMAX model is due to the terms identified with tail-reconnection, 34% to particle precipitation, and the remaining 17% from terms that appear to represent flowout. These losses are of SYM-H, not energy, and when estimating the transfer of energy, the factor of 2 in equation 2 must be taken into account. The 49% loss in SYM-H from tail-reconnection translates to a 74.5% loss in energy, primarily to the escaping plasmoid and Joule heating. This is roughly consistent with *Ieda et al.* [1998]; *Kamide and Baumjohann* [1993], who suggest approximate equipatition of energy between the ring current, the escaping plasmoid, and ionospheric Joule heating. Of the remaining 25.5% of the energy that enters the ring current, around a third (8.5%) is lost via the flowout terms, and two-thirds (17%) to particle precipitation. The loss due to particle precipitation is in line with a previous estimate of 12% by *Wang et al.* [2014].

7.7. Variability between model runs

To estimate the robustness of the results the NARMAX model was run 10 times, each time varying the selection of input data (see section 3). Figure 3 shows the relative magnitudes of the model terms for each model run, along with the overall accuracy of each model in reproducing the observed SYM-H. The data used in figure 3 are from 17 March 2000 to 9 May 2000, a period that was entirely excluded from the NARMAX algorithm in all of the model runs.

Figure 3a shows the ability of the model to predict SYM-H using only the measured solar wind parameters. The model SYM-H is calculated in an iterative manner, using previous *model* values of SYM-H with actual solar wind measurements, in the NARMAX model terms (table 1). In figure 3a the model samples are binned according to the SYM-H observations, with no less than 12 samples per bin. The colored patches represent the central 50% of the model samples in each bin. There is little difference between each of the models, especially at small to moderate -SYM-H where there are many samples. During these months in the spring of 2000, the models appear to systematically underestimate larger -SYM-H, but most of these samples occur in the declining phase of a single storm on the 6 April 2000 (see figure 4).

Figure 3b shows the variation in the magnetopause current terms of each model run. Run 1B produces a slightly smaller estimate of the magnetopause current contribution to SYM-H, but the narrow distributions (thin patches) indicate that the differences between model runs is primarily a scaling factor.

Figures 3c and 3d show the overall source and loss terms. The source terms are those associated with the magnetic field merging on the dayside (table 3), while the loss terms include particle precipitation (corresponding to τ in equation 6), tail reconnection (table 4), and flowout (table 5). The individual loss processes are broken down in figures 3e, 3f, and 3g.

While the overall source and loss rates are consistent across the model runs, there is a greater variation in the relative magnitude of each of the loss processes. The source of this variability comes from the nightside reconnection terms. This is not surprising, since internal magnetospheric processes are instrumental in triggering tail reconnection events (substorm onsets), which makes them difficult to model using only upstream solar wind measurements.

In the following section we show the NARMAX model output for three geomagnetic storms. For simplicity, and to avoid over-complicating the figures, only model results from the first run, 1A, are shown in these case studies. As figure 3 indicates, run 1A is representative of the models in general. The results from all model runs that include the flowout term are very similar, and lead to the same conclusions.

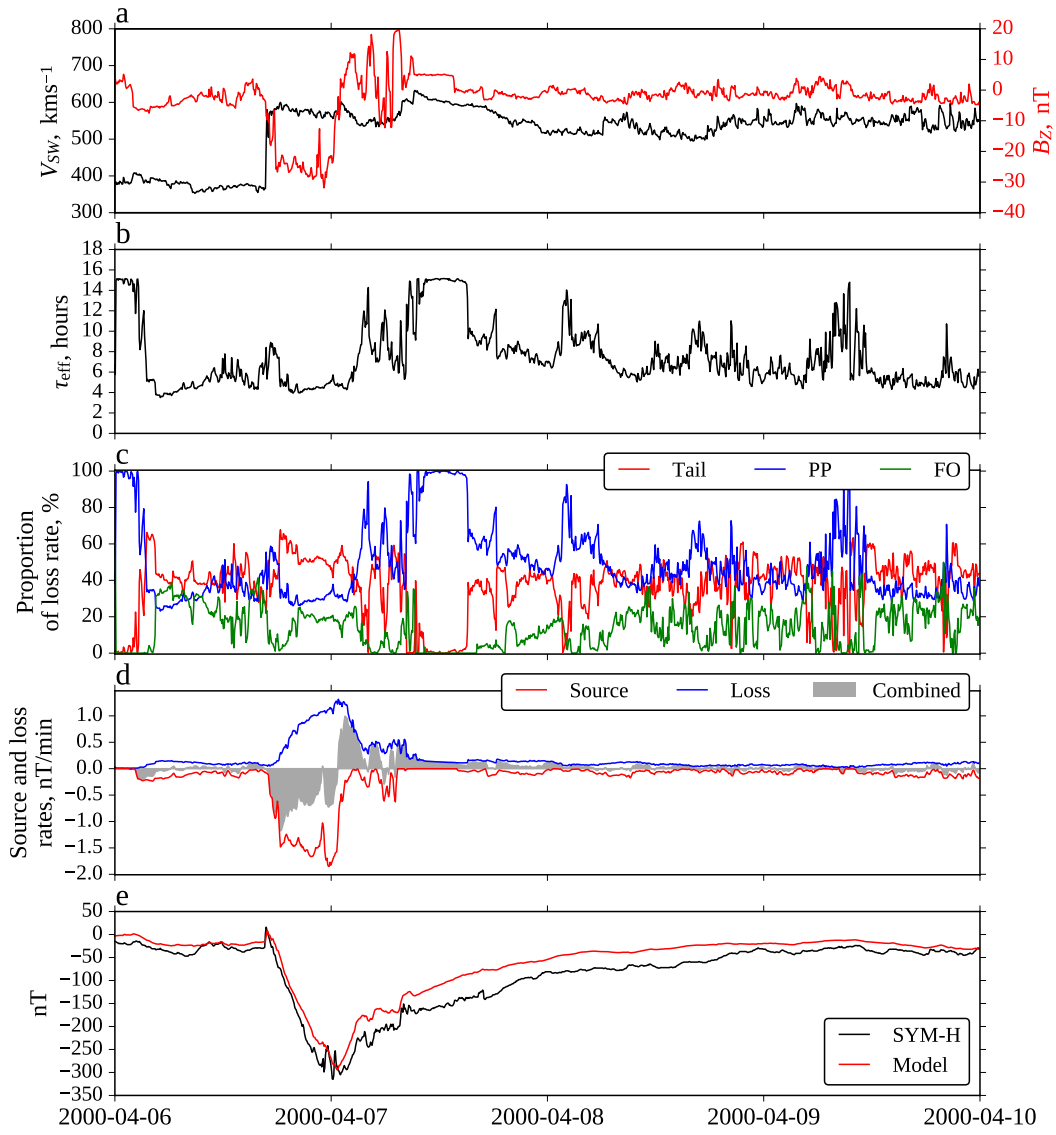

Figure 4. Results from the first run of the NARMAX model (run 1A), for the geomagnetic storm beginning 6 April 2000. Panel *a* shows the prevailing solar wind velocity and interplanetary magnetic field in the Z (GSM) direction. Panel *b* shows the effective exponential lifetime of SYM-H, in hours. In panel *c* the sizes of the loss terms are compared, where PP is particle precipitation/charge exchange, FO is flowout, and Tail is the loss of SYM-H from magnetotail reconnection. In *d* the total source (negative terms) and loss (positive terms) are compared. A comparison of the measured SYM-H values, and NARMAX predicted values is presented in *e*. Here the model results are calculated using only the solar wind measurements, and preceding model SYM-H, without any reference to measured values of SYM-H.

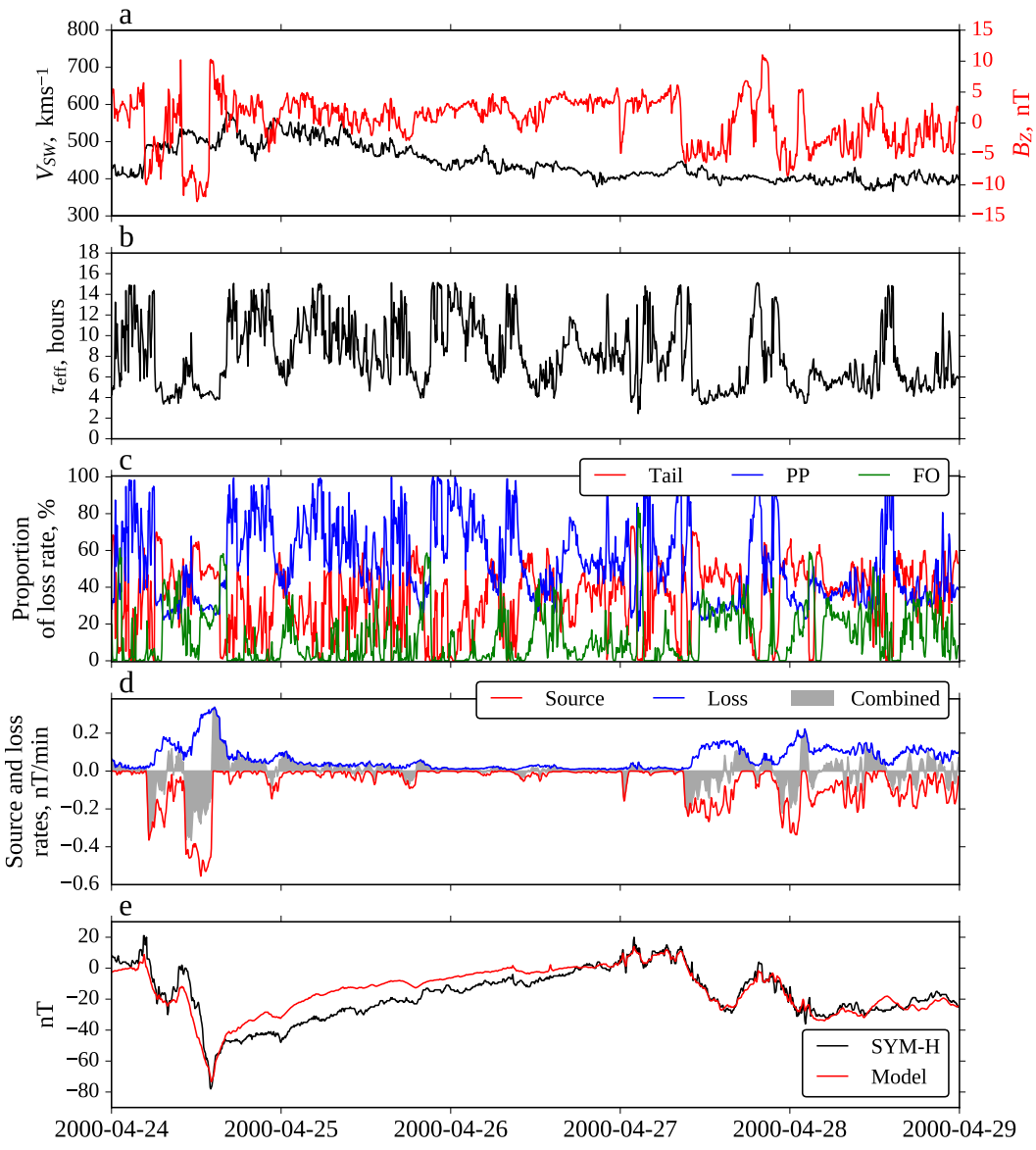

Figure 5. As figure 4, but for the storm beginning 24 April 2000.

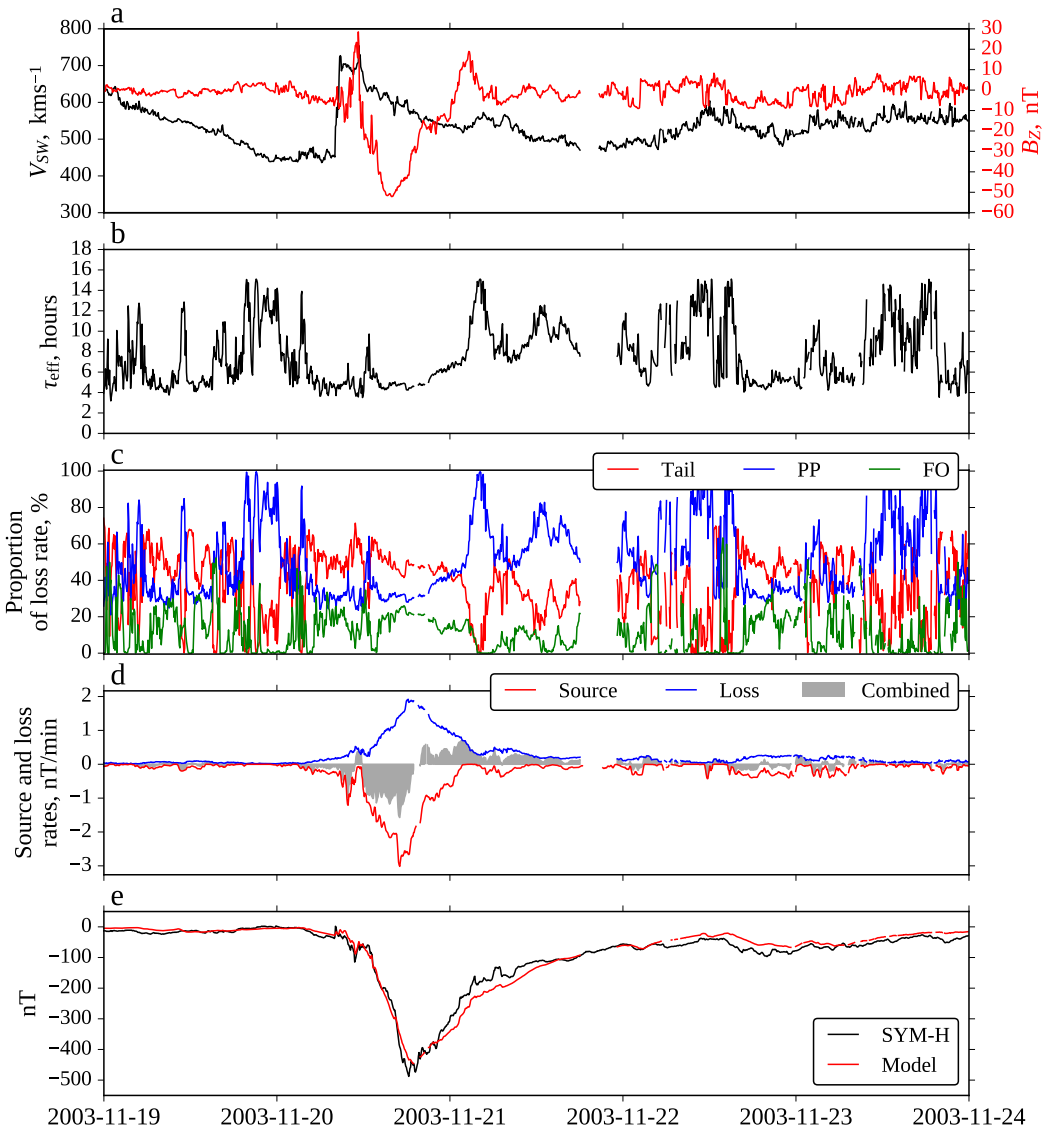

Figure 6. As figure 4, but for the storm beginning 20 November 2003.

8. Case studies

Figures 4, 5, and 6 show the results of NARMAX model run 1A during three geomagnetic storms, beginning on 6 April 2000, 24 April 2000, and 20 November 2003 respectively. Panel a shows the prevailing solar wind velocity and southward component of the IMF during the storms. The effective exponential decay time constant of SYM-H*, τ_{eff}, given in panel b, is based on the total SYM-H* loss rate, including flowout, tail re-

connection, and the purely exponential decay term of equation 6a. A breakdown of the percentage losses from each of these processes is given in panel c.

Panel d compares the magnitude of the source term with the combined loss term. The source is the merging of magnetic field on the dayside $-a\Delta\Phi_d$ (equation 6c), and has units of nT per minute. The shaded region shows the overall rate of change of SYM-H*, ie the combination of source and loss, also in nT per minute.

Panel e shows the measured value of SYM-H (black), and the model values (red). The model results are calculated iteratively using the NARMAX model terms to calculate the next value of SYM-H based on the previous model value, and solar wind data. The iteration begins at least 4 hours prior to the time period of interest, to allow it to converge and become independent of the starting value.

Each of the three events show a similar picture. At storm commencement, rapid increases in solar wind velocity and negative B_Z, are followed by an increase in the source term ($-a\Delta\Phi_d$), with a 20 to 30 minute lag. The losses of SYM-H increase much more slowly. Initially, and while the storm is being driven by the solar wind, the losses are mostly incurred in the tail reconnection (see panel c). During this time a large proportion of the SYM-H value comes from the distorted magnetotail. As the open magnetic field in the tail reconnects, most of the energy is lost to Joule heating, particle precipitation, and the plasmoid, and therefore the magnetotail contribution to SYM-H is not wholly replaced by the increase in ring current. In the declining phases of the storms the losses are mostly due to the idealized loss term, (equation 6a,) which is assumed to primarily represent charge exchange (particle precipitation) losses. These features, and the overall loss rate, match those given by the of the numerical model of *Kozyra and Liemohn* [2003]. It is clear from figure 5 panel d that the NARMAX model is capable of reproducing the smallest of changes seen in SYM-H, but the longer term decay following the storm is not as accurate. While the model makes good use of high resolution solar wind data, it lacks the complicated physics and wave-particle interactions that control acceleration and loss inside the magnetosphere.

Table 6. A performance comparison of SYM-H and Dst models.

Model	Parameter	RMSE (nT)	Correlation Coefficient
Average of three case studies. See figures 4, 5, and 6			
This study, run 1A	SYM-H	20.4	0.952
Burton et al. [1975]	Dst	38.1	0.894
Boynton et al. [2011a]	Dst	19.3	0.966
Temerin and Li [2002]	Dst	43.2	0.885
17 March 2000 to 9 May 2000.			
This study, run 1A	SYM-H	11.0	0.959
Burton et al. [1975]	Dst	14.5	0.891
Boynton et al. [2011a]	Dst	11.5	0.948
Temerin and Li [2002]	Dst	9.26	0.961

9. Performance of the model

The aim of this study is to quantify the individual physical processes involved in solar-wind – magnetosphere coupling, and identify their time lags, rather than produce a model for SYM-H. However, in this section we look at the performance of the model (run 1A) in reproducing SYM-H. For the three case studies in the previous section, the average RMSE of the model derived SYM-H is 20.4 nT, and the correlation coefficient is 0.952. For comparison, we have implemented the models of *Temerin and Li* [2002], *Boynton et al.* [2011a], and *Burton et al.* [1975], and provide the RMSE and correlation coefficients for each of the models in table 6. The models are also tested over the period 17 March 2000 to 9 May 2000. This time span is chosen because it has been excluded from the data used to produce all four of the models. Although *Temerin and Li* [2006] provides an updated version of the *Temerin and Li* [2002] model, it is not used here because it is trained on the data from this test period, giving it an unfair advantage. The present model compares favorably with the others, although it may be at a disadvantage due to the high time resolution of SYM-H, which could naturally lead to higher RMSE than the low resolution Dst index. The model of *Temerin and Li* [2002] is by far the most complicated of the four models. It performs very well overall, but poorly for the large storm of the third case study (20 November 2003).

10. Summary

There are some limitations in the method and results of the models presented in this study. Firstly, the NARMAX algorithm can only select from finite set of candidate predictors. Some coupling processes might not be well represented by any of the available choices. This is likely the case with the model flowout terms. The actual flowout rate depends on multiple different lags of solar wind parameters, these determine the density of ring current particles, and control the dayside loss rate of those particles by altering the location of the magnetopause. Secondly, the maximum lag time in the models is 4 hours. Some magnetospheric processes take longer than this. For example, high energy (MeV) particles respond with 5 to 40 hour delays to solar wind enhancements [*Li et al.*, 2005]. These particles are energized in different processes to the lower energy particles that dominate the ring current. However, their populations are too small to significantly affect SYM-H.

Despite these limitations, the NARMAX algorithm has produced models that accurately reproduce SYM-H, while quantifying several of the individual coupling processes, and providing their lag times. According to the NARMAX models, the lag time between the merging of the IMF and geomagnetic field, and the increase tail currents from the stretched magnetotail is 20 to 30 minutes. The lag time from dayside merging to magne-

totail reconnection is 60 to 120 minutes. These times match the impulse response of the AL index to changes in solar wind vB_S, which is observed to have two peaks at 20 min and 60 min [*Bargatze et al.*, 1985]. Note that although tail reconnection causes a decay in -SYM-H, this is not the case with the AL index, which responds positively to substorm expansion.

It is difficult to say which of the model runs will provide the truest representation of any particular geomagnetic storm. There are slight variations in the performance of the models depending on the particular event. The most significant difference between the models is the division of losses between the different loss mechanisms. Any of the models that include the flowout loss term (ie models 1A, 1B, 2A, 4A, 4B, or 5A) should be equally valid, within the errors of this investigation. We would recommend using model 1A, for ease of comparison with the results of this study, and because it provides values of SYM-H slightly closer to the measurements during the largest storms.

The models provide empirical evidence for the theory of *Vasyliūnas* [2006], namely that the negative swings in Dst and SYM-H, which are described by the well known coupling functions, are firstly an observation of the open geomagnetic field piling up in the magnetotail and enhancing cross-tail currents. When particles are injected on the nightside during tail reconnection, -SYM-H decays. This is because the loss of -SYM-H from the dipolarization of the geomagnetic tail is greater than the gain in -SYM-H from the particle injection. Although *Vasyliūnas* [2006] expected the effects of dipolarization and injection to almost cancel, this result is in agreement with other studies [*Iyemori and Rao*, 1996; *Siscoe and Petschek*, 1997].

Acknowledgments. This work was supported by the Natural Environmental Research Council grant NE/J007773/1. The OMNI data are available from the GSFC/SPDF OMNIWeb interface at http://omniweb.gsfc.nasa.gov. SYM-H data is available from the World Data Center for Geomagnetism, Kyoto, at http://wdc.kugi.kyoto-u.ac.jp/.

References

Bargatze, L. F., D. N. Baker, R. L. McPherron, and E. W. Hones (1985), Magnetospheric Impulse Response for Many Levels of Geomagnetic Activity, *J. Geophys. Res.*, *90*, A7, 6387–6394.

Billings, S. A., and H. L. Wei (2005), he wavelet narmax representation: A hybrid model structure combining polynomial models with multiresolution wavelet decompositions, *Int. J. Systems Science*, *36*, 137–152.

Billings, S. A. (2013), Nonlinear System Identification: NARMAX Methods in the Time, Frequency, and Spatio-Temporal Domains, John Wiley & Sons, ISBN 978-1-119-94359-4.

Boynton, R. J., M. A. Balikhin, S. A. Billings, A. S. Sharma, and O. A. Amariutei (2011), Data derived NARMAX Dst model, *Ann. Geophysicae*, *29*, 965 – 971, doi:10.5194/angeo-29-965-2011.

Boynton, R. J., M. A. Balikhin, S. A. Billings, H. L. Wei, and N. Ganushkina (2011), Using the NARMAX OLS-ERR algorithm to obtain the most influential coupling functions that affect the evolution of the magnetosphere, *J. Geophys. Res.*, *116*, A05218, doi:10.1029/2010JA015505.

Burton, R. K., R. L. McPherron, and C. T. Russell (1975), An empirical relationship between interplanetary conditions and Dst, *J. Geophys. Res.*, *80*, 4204–4214.

Dessler, A. J., and E. N. Parker (1959), Hydromagnetic theory of magnetic storms, *J. Geophys. Res.*, *64*, 2239–2259.

Dusik, S., G. Granko, J. Safrankova, Z. Nemecek, and K. Jelinek (2010), IMF cone angle control of the magnetopause location: Statistical study, *Geophys. Res. Lett.*, *37*, L19103, doi:10.1029/2010GL044965.

Hoffmann, W. (1989), Iterative algorithms for Gram-Schmidt orthogonalization, *Computing*, *41*(4), 335–348.

Hong, X. and C. J. Harris (2001), Nonlinear model selection structure detection using optimum experimental design and orthogonal least squares, *IEEE Transactions on Neural Networks 12* (2), 435–439.

Ieda, A., S. Machida, T. Mukai, Y. Saito, T. Yamamoto, A. Nishida, T. Terasawa, and S. Kokubun (1998), Statistical analysis of the plasmoid evolution with Geotail observations *J. Geophys. Res.*, *103*, A3, 4453–4465.

Iyemori, T., and D. R. K. Rao (1996), Decay of the Dst field of geomagnetic disturbance after substorm onset and its implication to storm – substorm relation, *Ann. Geophysicae*, *14*, 608 – 618.

Kamide, Y., and W. Baumjohann (1993), Magnetosphere-Ionosphere Coupling, Springer-Verlag, New York, ISBN: 978-3-642-50064-0.

Kan, J. R., and L. C. Lee (1979), Enery coupling and the solar wind dynamo, *Geophys. Res. Lett.*, *6*, 577.

King, J. H., and N. E. Papitashvili (2006), Solar wind spatial scales in and comparisons of hourly Wind and ACE plasma and magnetic field data, *J. Geophys. Res.*, *110*, A02104, doi:10.1029/2004JA010649.

Kozyra, J. U., and M. W. Liemohn (2003), Ring current energy input and decay, *Space Sci. Reviews.*, *109*, 105–131.

Lopez, R. E., W. D. Gonzalez, V. Vasyliūnas, I. G. Richardson, C. Cid, E. Echer, G. D. Reeves, P. C. Brandt (2015), Decrease in SYM-H during a storm main phase without evidence of a ring current injection, *J. Atmos. Sol.-Terr. Phys.*, *134*, 118–129, doi:10.1016/j.jastp.2015.09.016

McPherron, R. L., and T. P. O'Brien (2001), Predicting geomagnetic activity: The Dst index, *Space Weather, Geophys. Monogr. Ser.*, *125*, edited by P. Song, H. Singer, and G. Siscoe, 339–345.

Sckopke, N. (1966), A general relation between the energy of trapped particles and the disturbance field near Earth, *J. Geophys. Res.*, *71*, 3125.

Scurry, L., and C. T. Russell (1991), Proxy studies of energy transfer to the magnetopause, *J. Geophys. Res.*, *96*, 9541.

Siscoe, G. L. (1970), A Virial Theorem Applied to Magnetospheric Dynamics, *J. Geophys. Res.*, *75*, 28, 5340–5350.

Siscoe, G. L., and H. E. Petschek (1997), On storm weakening during substorm expansion phase, *Ann. Geophysicae*, *15*, 211–216.

Tanskanen, E. I. (2002), Terrestrial substorms as a part of global energy flow, *FMI Contributions* (36), ISBN 952-10-0423-1.

Temerin, M., and X. Li (2002), A new model for the prediction of Dst on the basis of the solar wind, *J. Geophys. Res.*, *107*, A12, 1472, doi:10.1029/2001JA007532.

Temerin, M., and X. Li (2006), Dst model for 1995 – 2002, *J. Geophys. Res.*, *111*, A04221, doi:10.1029/2005JA011257.

Vasyliūnas, V. M. (2006), Reinterpreting the Burton-McPherron-Russell equation for predicting Dst, *J. Geophys. Res.*, *111*, A07S04, doi:10.1029/2005JA011440.

Vasyliūnas, V. M. (2006), Ionospheric and boundary contributions to the Dessler-Parker-Sckopke formula for Dst, *Ann. Geophysicae*, *24*(3), doi:10.5194/angeo-24-1085-2006.

Wang, C., J. P. Han, H. Li, Z. Peng, and J. D. Richardson (2014), Solar wind-magnetosphere energy coupling function fitting: Results from a global MHD simulation *J. Geophys. Res. Space Physics*, *119*, 6199–6212, doi:10.1002/2014JA019834.

Wanliss, J. A. and K. M. Showalter (2006), High-resolution global storm index: Dst versus SYM-H, *J. Geophys. Res.*, *111*, A02202, doi:10.1029/2005JA011034.

Wygant, J. R., R. B. Torbert, and F. S. Mozer (1983), Comparison of S3-3 polar cap potential drops with the interplanetary magnetic field and models of magnetic reconnection, *J. Geophys. Res.*, *88*, 5727.

Li, X., D. N. Baker, M. Temerin, G. Reeves, R. Friedel, and C.Shen (2005), Energetic electrons, 50 keV to 6 MeV, at geosynchronous orbit: Their responses to solar wind variations, *Space Weather*, *3*, S04001, doi:10.1029/2004SW000105.

Zieba, A. (2010), Effective number of observations and unbiased estimators of variance for autocorrelated data – an overview, *Metreology and Measurement Systems*,*XVII*(1), 3–16. DOI: 10.2478/v10178-010-0001-0.